

Lessons from the first multiply imaged supernova: A revised Light-Traces-Mass strong lensing model for the galaxy cluster MACS J1149.5+2223

ADI ZITRIN¹

¹*Physics Department, Ben-Gurion University of the Negev, P.O. Box 653, Be'er-Sheva 84105, Israel*

(Received; Revised; Accepted)

Submitted to ApJ

ABSTRACT

Our light-traces-mass (LTM) strong-lensing model for MACS J1149.5+2223 has played several key roles over the last decade: it aided the identification of multiple images in this cluster and the study of MACS1149-JD1 at redshift $z \simeq 9$, it was used to estimate the properties of the first multiply imaged supernova, Refsdal, in its discovery paper, and of the first caustic crossing event by a cluster, Lensed Star 1. Supernova Refsdal supplied an invaluable opportunity to conduct a blind test of the ability of common lens-modeling techniques to accurately describe the properties of SN Refsdal's images and predict the reappearance of one of its counter images that was due about a year post-discovery of the original Einstein cross. Thanks to this practice, in which our submitted model yielded some outlying results, we located a numerical artifact in the time delay (TD) calculation part of the code, which was now fixed. This artifact did not influence the reproduction of multiple images (i.e., the deflection fields – which are those constrained directly from the observations) or the derived mass model, and so it remained unnoticed prior to supernova Refsdal, emphasizing the importance of blind tests in astronomy. Here we update our model and present revised LTM measurements for Refsdal. These are important not only for completing the LTM view of the Refsdal event, but also because they affect the range of values predicted from different lens-modeling techniques and thus the range of systematic uncertainties for the TD calculation and the resulting Hubble constant.

Keywords: cosmology: observations – cosmology: cosmological parameters – galaxies: clusters: general – galaxies: clusters: individual: MACS J1149.5+2223 – gravitational lensing: strong

1. INTRODUCTION

Measuring the expansion rate of the Universe and the Hubble constant in particular has been one of modern astronomy's Holy Grails.

More than 50 years ago, Refsdal (1964) suggested a way to measure the Hubble constant using a multiply imaged supernova (SN). Since light rays to each multiple image traverse a different path and cross a different potential well, each image has a different, delayed arrival time. The difference in arrival times, i.e., the time delay difference (which we refer to here, in short, simply as the time delay; TD), is inversely proportional to the Hubble constant. Hence, by measuring the TD between multiple

images of the exploding SN, a measurement of the Hubble constant would be enabled (assuming a lens model is at hand, e.g., from the position of the observed SN images). In fact, Refsdal's idea applies to a wider range of observable transients. More commonly, thanks to their brightness and the fact that they are not short lived, multiply imaged quasars – typically lensed by galaxies and monitored over a long time-span – have been used to derive accurate estimates of the Hubble constant (e.g., Vuissoz et al. 2008; Suyu et al. 2013; Wong et al. 2019, the latter finding $H_0 = 73.3^{+1.7}_{-1.8}$ km/s/Mpc). Such measurements have recently gained an additional interest as, together with constraints from improved Cepheid measurements to Type Ia SNe (e.g., Riess et al. 2019, $H_0 = 74.03 \pm 1.42$, km/s/Mpc), they seem to be in tension with the values derived from Planck's observations of the cosmic microwave background (CMB; Planck Col-

laboration et al. 2018), which favor a smaller value of 67.4 ± 0.5 km/s/Mpc. This discrepancy could possibly hint to new physics (e.g., Blandford et al. 2020), but various systematics, such as those manifested in the discrepancy between the local value from Cepheids and that from Tip of the Red Giant Branch calibration (Freedman et al. 2019, $H_0 = 69.8 \pm 0.8 \pm 1.7$ km/s/Mpc), have to be understood first.

Due to their relative short duration and typical rate, up until a few years ago multiply imaged SNe have not, in fact, been detected at all and thus were not used to constrain H_0 . About five years ago and fifty years after Refsdal’s original prediction, the first clear example of a multiply imaged SN was discovered (Kelly et al. 2015), as an Einstein cross around a cluster member in the field of the galaxy cluster MACS J1149.5+2223 (M1149 hereafter, Ebeling et al. 2007). As a courtesy to the original paper, the SN was dubbed *SN Refsdal*. A couple of other multiply imaged SNe have also been detected: an apparently bright SN, multiply-imaged by a galaxy was noted in the year preceding Refsdal (PS1-10afx; Quimby et al. 2013, 2014), albeit it was not resolved into multiple images and a TD was not measured for it; and the first multiply imaged Type Ia SN, also lensed by a galaxy, was later discovered (iPTF16geu; Goobar et al. 2017). SN Refsdal appears to have exploded in an arm of a spiral galaxy multiply imaged by the cluster, M1149, and further, more locally, by a cluster member. Being clearly resolved and lensed by a cluster so that an additional appearance of the SN was predicted roughly a year after the detection of the Einstein cross (Kelly et al. 2015, 2016), SN Refsdal opened a unique door for both predicting when a future SN explosion could be observed, and, for measuring H_0 . In addition, it allowed for a true blind comparison test of various lens modeling techniques – or the parametrization of the underlying mass density – to accurately predict the reappearance (Treu et al. 2016; Rodney et al. 2016a; Kelly et al. 2016).

The galaxy cluster M1149 was detected thanks to its X-ray signal as part of the MAAssive Cluster Survey (MACS; Ebeling et al. 2007). The first lensing analysis of M1149 was published around the same time by Zitrin & Broadhurst (2009), who proposed many of the gold multiple images in this cluster (see Table 2), and by Smith et al. (2009), who also measured spectroscopically the redshift for some of these systems. Following its compelling features, M1149 was also observed in 16 bands as a high-magnification cluster in the Cluster Lensing And Supernova survey with Hubble treasury program (CLASH; Postman et al. 2012), and included in the subsequent ultra-deep Hubble Frontier Fields program (HFF; Lotz et al. 2017), and in the Grism Lens-

Amplified Survey from Space (GLASS; Treu et al. 2015). It has also been a part of extensive ALMA programs, such as the ALMA Frontier Fields survey (PI: Bauer; e.g., González-López et al. 2017), or the ALMA Lensing Cluster Survey (ALCS; PI: Kohn). Following this rich coverage, including ground based spectroscopy (e.g., Treu et al. 2016 and references therein) many other lens models for the cluster have been published to date (e.g., Rau et al. 2014; Richard et al. 2014; Johnson et al. 2014; Kawamata et al. 2016; Diego et al. 2016, see also the HFF webpage ¹).

M1149 has been the at the heart of a wide variety of studies, from high-redshift galaxies (e.g., Zheng et al. 2017; Ishigaki et al. 2018) or ultra diffuse galaxies (e.g., Janssens et al. 2019), through lensed galaxy properties (e.g., Wang et al. 2017; Muñoz Arancibia et al. 2018; Carvajal et al. 2020) and their ionizing photon budget (e.g., Emami et al. 2020), to finding AGN in cluster fields (e.g., Della Costa et al. 2020); as a few random examples. In addition, M1149 is known to host several record-breaking phenomena: aside from lensing the first resolved multiply imaged SN, it has been found, for example, to host one of the highest redshift galaxies known (Zheng et al. 2012) later verified spectroscopically to become the farthest Lyman-alpha emitter to date (Hashimoto et al. 2018); it allowed the plausible detection of a $\sim 10^{10} M_\odot$ black hole near the center of the brightest cluster galaxy (BCG; Chen et al. 2018); and it allowed the first detection of a cosmological caustic crossing event by a cluster, dubbed MACS J1149 Lensed Star 1 (MACS1149-LS1; also known as Icarus; Kelly et al. 2018). The latter was detected in follow-up observations of SN Refsdal, and consists, most likely, of a young massive star in an arm of the same spiral galaxy hosting Refsdal at $z = 1.49$ that crosses the caustics (Kelly et al. 2018). This detection has opened the door for finding more such transients in other clusters that were relatively frequently visited with HST (Chen et al. 2019; Rodney et al. 2018; Kaurov et al. 2019).

Over the past decade our Light-Traces-Mass (LTM) model for M1149, updated various times throughout, has played some key roles in studies of this cluster, from finding some of the first multiple images (Zitrin & Broadhurst 2009), through aiding in qualifying it for the HFF via simulations of high-redshift galaxy expectations (section 3 in Lotz et al. 2017), to helping in the investigation of MACS1149-JD1 (Zheng et al. 2012), SN Refsdal (Kelly et al. 2015), or MACS1149-LS1 (Kelly et al. 2018; Diego et al. 2018). Our goal here is to

¹ <https://archive.stsci.edu/prepds/frontier/lensmodels/>

present a long-due update of the model. In particular, we take advantage of the blind comparison work by [Treu et al. \(2016\)](#); [Rodney et al. \(2016a\)](#); [Kelly et al. \(2016\)](#) that examined the ability of common lens modeling techniques to predict the reappearance and properties of SN Refsdal, and in which our submitted model yielded some outlying estimates – especially regarding the Einstein cross. This experiment has led us to detect a very minor, but apparently critical, numerical inconsistency in the TD calculation part in our code. We fix this so-called error and show that the model we submitted blindly before does in fact reproduce a reasonable TD surface for SN Refsdal. We update the model, and publish here new LTM measurements for SN Refsdal. While preliminary estimates of the TD have been presented in [Treu et al. \(2016\)](#); [Rodney et al. \(2016a\)](#); [Kelly et al. \(2016\)](#), no such information is used in the minimization. Finally, we briefly discuss the implications on the Hubble constant, H_0 , of our new TD measurement (e.g., [Vega-Ferrero et al. 2018](#); [Grillo et al. 2018](#)).

M1149 will also be included in various JWST/GTO programs², and more exciting science is thus expected in this cluster in the near future. Our model is made publicly available³. A future version of the model, over a larger field of view, is expected in the framework of the Beyond Ultra-deep Frontier Fields and Legacy Observations (BUFFALO; [Steinhardt et al. 2020](#)) program with Hubble.

The paper is organized as follows: in §2 we give a short overview of the LTM methodology and in §3 we outline our modeling of M1149. In §4 we present and discuss the results from this modeling with an emphasis on SN Refsdal, namely the magnification ratios, TDs, and implications for the Hubble constant. The work is concluded in §5. Throughout this work we use a Λ CDM cosmology with $\Omega_M = 0.3$, $\Omega_\Lambda = 0.7$, and $H_0 = 70$ km/s/Mpc. Unless otherwise stated, errors are 1σ , and we generally use AB magnitudes ([Oke & Gunn 1983](#)).

2. THE LTM CODE

The LTM code relies on the assumption that light traces mass, so that the weighted luminosity distribution of cluster galaxies can act as a guide for the shape of the total matter distribution. A first version of the code was written and used by [Broadhurst et al. \(2005\)](#) to find dozens of multiple images in Abell 1689, revealing a very large lens. Based on their success, [Zitrin](#)

[et al. \(2009\)](#) developed a new, simpler LTM code that included a minimal number of free parameters. This code was since constantly improved, and used to identify multiple images and model dozens of galaxy clusters. Perhaps the greatest value of the code lies in that it is frequently successful in predicting the location of multiple images based only on the luminosity distribution of cluster members, even before it is constrained with any multiple image systems ([Carrasco et al. 2020](#), see also [Zalesky & Ebeling \(2020\)](#)). A second importance is that it is distinct from typical, analytic lens modeling techniques and thus probes a different range of solutions. We give here a brief overview of the code; for more details see [Zitrin et al. \(2015\)](#), see also [Carrasco et al. 2020](#).

The starting point of the model is the distribution of cluster members and their luminosities. Each galaxy is assigned with a power-law mass density profile, scaled in proportion to its luminosity. The power-law exponent is a free parameter of the model and the same for all galaxies. A grid is defined – typically matching a portion of the HST image of the cluster – and the total deflection field and mass density distribution of the galaxies are calculated on that grid. This galaxies’ map is then smoothed (in Fourier space) with a Gaussian kernel to produce a map of the dark matter component. The width of the Gaussian is a free parameter as well. The deflection field maps from the galaxies and the DM are then added with a relative weight, which is also a free parameter of the model, and supplemented by a two component external shear whose strength and position-angle parameters are typically left free to be optimized as well. The overall normalization of the model is the sixth free parameter.

In addition, we often leave free the core size, relative weight (i.e., the relative mass-to-light ratio), ellipticity and position angles of key cluster members, such as the BCGs. All other member galaxies are assumed to be circular and core free, for simplicity.

The optimization of the model is carried out by minimizing a χ^2 function that measures the distance of predicted multiple images from their observed location, via a Monte-Carlo Markov Chain with a Metropolis-Hastings algorithm. Punishing terms can be added for images with wrong parity or if extra images are predicted. We also include some annealing in the procedure, and the chain typically runs for several thousand steps after burn-in phase. Errors are typically calculated from the same Markov chain.

3. LTM MODELING OF M1149

As mentioned, the first SL LTM model for M1149 was constructed in 2009 with an old code, prior to CLASH

² <https://www.stsci.edu/jwst/observing-programs/approved-gto-programs>

³ <https://www.dropbox.com/sh/mac3vuiian8gyjkq/AADTD0ENfwwclj9GJHnUhua?dl=0>

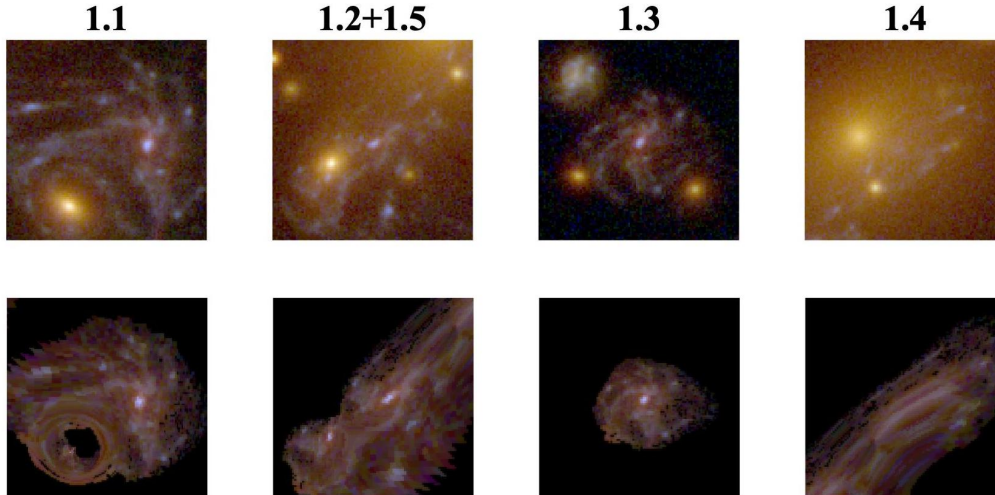


Figure 1. Reproduction of system 1 by our model. We send image 1.1 to the source-plane and back to obtain the reproduction of the other images of this system. The first stamp is $7.8''$ on $7.8''$ and the three other stamps are $6.5''$ on $6.5''$.

multiband data, and before redshifts were available for this cluster. This model was later updated with improvements to the code and using CLASH data or newer products agreed on within the HFF framework, and included strong lensing, or strong+weak lensing constraints combined (e.g. Zitrin et al. 2015; Treu et al. 2016; Zheng et al. 2017). Here, we update the model submitted to the Treu et al. (2016), Kelly et al. (2016) and Rodney et al. (2016a) blind tests, with a corrected TD calculation (see §4.2).

Since the model is limited to the grid resolution and our goal here is to examine the properties of SN Refsdal, we concentrate on the central $\sim 140'' \times 140''$ area of the cluster. The final model has the same spatial resolution as the model presented in Treu et al. (2016), of $0.''065/\text{pix}$, native to the public CLASH HST images (although some parts in the minimization are done in a few-times lower resolution for speed-up purposes).

We leave the weight of four galaxies free: the central BCG (RA=11:49:35.70, DEC=+22:23:54.71); a second bright cluster member at RA=11:49:37.55, DEC=+22:23:22.49; another bright member next to the center at RA=11:49:36.86, DEC=+22:23:46.97; and the galaxy that lenses SN Refsdal into the Einstein cross (RA=11:49:35.47, DEC=+22:23:43.63). The ellipticity and position angle of the main BCG are left free to be optimized around their values measured by SExtractor (Bertin & Arnouts 1996), and the ellipticity and position angle of the second and third BCGs are kept fixed on their measured values. A core is assumed for the central BCG, whose size is a free parameter. The general

galaxy power-law parameter, q , is fixed to 1.45, based on various trials that have shown that this value works very well in reproducing the partial spiral counter image north of the BCG (see Fig. 1).

The multiple image constraints we use here are given in Table 2. These consist mainly of the *gold* multiply imaged systems presented in Treu et al. (2016) and Finney et al. (2018), with some *silver* counter images that our model predicts as secure. The *gold/silver/etc.* ranking was given based on voting by lens modelling teams in the framework HFF and SN Refsdal’s efforts (Treu et al. 2016, for details). We also adopt the detailed mapping of the main, lensed spiral galaxy’s internal knots as presented in Treu et al. (2016, and references therein) and Finney et al. (2018), and use these as additional constraints, as listed in Table 3. All systems were fixed to their spectroscopic redshift where available. System 6 & 7 do not have a spectroscopic measurement and their redshift was fixed to $\simeq 2.6$ based on their photo- z . We do not use any measured TDs or magnification ratios as input.

For the χ^2 calculation, a positional uncertainty of $0.5''$ is adopted for most multiply images, but for the four SN images in the Einstein cross we adopt $0.1''$. We also include punishing terms to guarantee the correct parity of these images, and to verify that no additional (full) image of the spiral galaxy is predicted just north of the BCG, which was the case in some trial models.

4. RESULTS

Our resulting mass model is seen in Fig. 2, along with the magnification map and TD surface contours. The

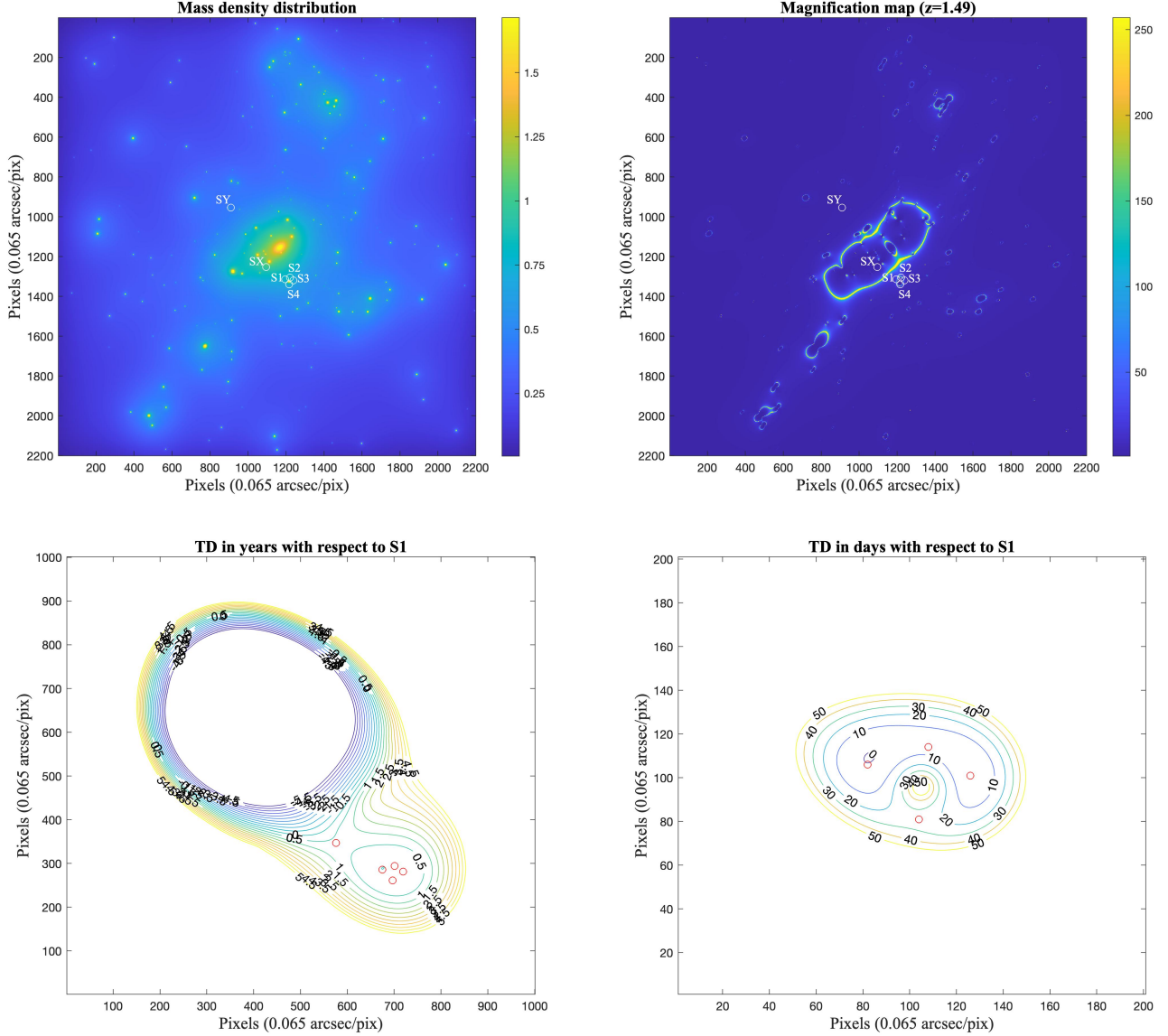


Figure 2. Our revised LTM SL model for M1149. *Upper left* figure shows the surface mass density, κ , for the redshift of system 1, the spiral galaxy at $z = 1.49$, with the positions of S1-S4, SX, and SY, marked with white circles; the *Upper right* figure shows the magnification map for that redshift, similarly marking the SN image positions; the *Bottom left* figure shows contours of the TD surface with respect to the SN image S1, in decrements of 0.5 years, marking with red circles the Einstein cross images and SX; the *Bottom right* figure shows contours of the TD surface with respect to the SN image S1, in decrements of 10 days, marking with red circles the positions of the Einstein cross images.

final model has an image reproduction rms of $0.68''$, and a $\chi^2 \simeq 242$. With the many multiple images used, the number of constraints is $N_c = 170$, and the number of free parameters $N_p = 11$, such that the number of degrees of freedom is $DOF = N_c - N_p = 159$. Hence the *reduced* χ^2 is $\simeq 1.5$. We note that for the spiral knots alone the rms is a bit lower, $0.49''$ (note also the rms is limited by the grid's resolution; a quantification of this effect will be done elsewhere).

The reproduction of the complex configuration of system 1 can also constitute a (more qualitative, in our case) testimony for the model's credibility in the central region. We show the reproduction of this system in Fig. 1, compared to the data, by sending the largest spiral image to the source-plane and back. The reproduction of some knots is not very prominent, perhaps indicative of some inaccuracy or a resolution limit, although

overall the model seem to predict very well the detailed appearance of the images.

4.1. LTM TDs and magnifications for SN Refsdal

The model’s TDs and magnification ratios, with respect to S1, for SN Refsdal’s five observed images (S1-S4 and SX), as well as the older unobserved SN image (SY), are given in Table 1. The quoted errors were derived using a 100 random models from a designated MC chain, and we list both the 68.3% and 95% confidence intervals. To account for (some) systematics, these were extracted using an effective $\sigma_{pos} \simeq 1.7''$, which we have found better captures the range of values from different trial models constructed in the course of modelling M1149. The original statistical intervals are about 3-5 times smaller. The relevant values seem to broadly agree, in most cases, with the early measurements by Rodney et al. (2016b) and Kelly et al. (2016), listed in the same table as well. However, we anticipate that updated measurements for SN Refsdal, exploiting a wider monitoring time-span of Refsdal’s appearances, will become available in the future. While a major discrepancy between such updated measurements and our current estimate may persist, we note that our numbers seem to very broadly agree with the range of estimates from the different models seen in Rodney et al. (2016b), Treu et al. (2016), and Kelly et al. (2016). Most models predict TDs of order days for S2 and S3 with respect to S1; about 15-30 days between S4 and S1, and from ~ 220 to ~ 380 days between SX and S1. Nevertheless, it seems that LTM TD estimates, and most notably for the SX-S1 TD, are systematically lower than those obtained by most parametric techniques. In addition, if updated SX-S1 TD measurements remain significantly different than our estimate, it can potentially cast important clues on properties of the underlying matter distribution that are critical for TD mapping. Based on the early measurements by Kelly et al. (2016) the TD is not very likely to be shorter than our estimate (see also Baklanov et al. 2020), and is more likely to be significantly larger: following Kelly et al. (2016) SX was detected on 11 December 2015, and shows fainter traces also on 14 November 2015 – almost exactly a year after detecting the Einstein cross on 10 November 2014. In contrast, observations from 30 October 2015 yielded no statistically significant detection of SX. Hence, as seen in Fig. 3 in Kelly et al. (2016), unless the magnification of SX is very small compared to S1, most chances are that the SX-S1 TD is larger than our estimate of ~ 267 days (or ~ 224 days, depending on the source position).

The absolute magnifications are not listed in Table 1, and instead given here. Our model predicts magnifications of $\mu \sim 20 - 22$ for the images S1-S3, $\mu \simeq 5.2$ for S4,

and $\mu \simeq 4.7$ for SX. SX is predicted at RA=177.39995, DEC=22.39664 by our model, about $\simeq 0.4''$ from its observed location in Kelly et al. (2016). The model suggests that SY appeared $\simeq 18$ years ago, with a magnification of $\mu \sim 3.4$.

It is worth mentioning that in the presented model, the effective ellipticity of the galaxy that forms the Einstein cross was not optimized separately; the galaxy was modeled as a simple circular power-law, and the ellipticity of its critical curve, which produces the four images of the SN, was automatically obtained as such likely due to the shear caused by the main potential well, centered on the BCG. It is conceivable that an independent modeling of this lensing galaxy could yield more refined results. Similarly, we remind the reader that the LTM code is limited to the grid’s resolution, which could affect the TD measurement. To assess the typical magnitude of the effect, we repeat the TD measurements from our model with a resolution twice lower in each axis. The TDs between the images of the Einstein cross change by about few to ~ 10 days (and so the estimate for the order of images S1-S3 can also change), and the TD between SX and S1, as well as the confidence interval, increase by about a month. As for the magnification ratios, while most typically agree within $1-2\sigma$ with the higher resolution result, some may be more severely affected – especially those images near the critical curve (i.e., the Einstein cross images) and the higher-resolution results are needed to obtain more stable predictions for them. In cases where very high-resolution results are needed, analytic codes (which essentially can obtain any desired resolution) may be preferable, although in some cases higher-resolution grids could also be employed with LTM.

Note that since the TDs are affected by the exact position of the source (e.g., Birrer & Treu 2019), we quote in Table 1 values for two cases: in the first the source position is taken as the average delensed position of the four SN images of the Einstein cross, similar to what was done prior to the appearance of SX. For comparison, and although SX is not used in the minimization, we also list the estimates if the source position is taken as the mean delensed position of both the four Einstein cross images and SX. As can be seen, most properties agree fairly well (although sometimes marginally) within the errors between the two scenarios, but for some cases the effect on the TD and arrival order can be more significant. The TDs quoted by the first source position is probably more representative of the properties of S1-S4, whereas it remains to be seen if the TD taken from the second source position including SX, describes better the SX-S1 TD, as one may speculate. In that sense the *first* SX-S1

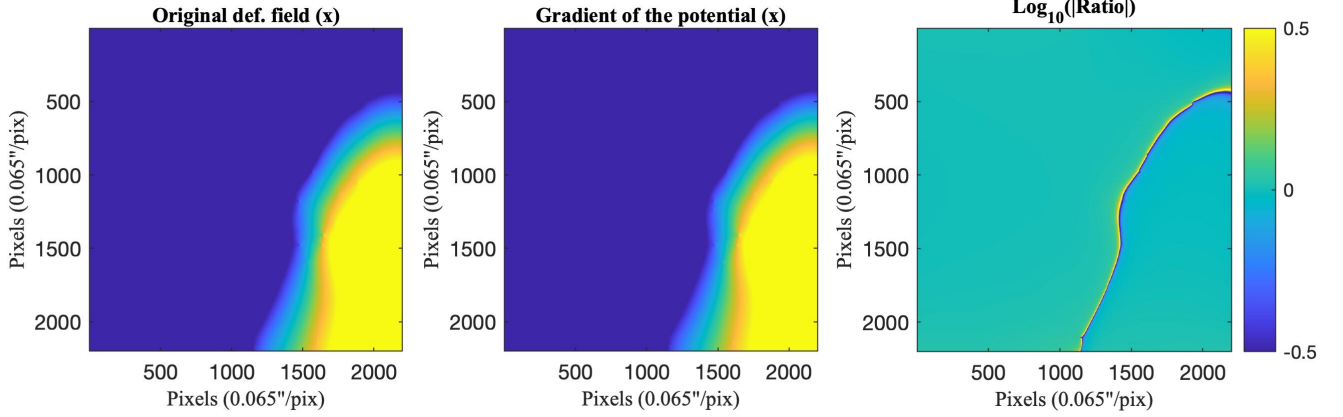


Figure 3. Residual from the calculation of the numerically-integrated potential. *Left:* The original best-fit x-axis deflection field. *Center:* The derived x-axis deflection field obtained from the gradient of the (numerically-integrated) potential. *Right:* \log_{10} of the absolute value of the ratio of the two deflection fields. While the ratio equals unity in most of the field, a numerical residual is clearly seen. Values were limited to ± 0.5 to emphasize the artifact.

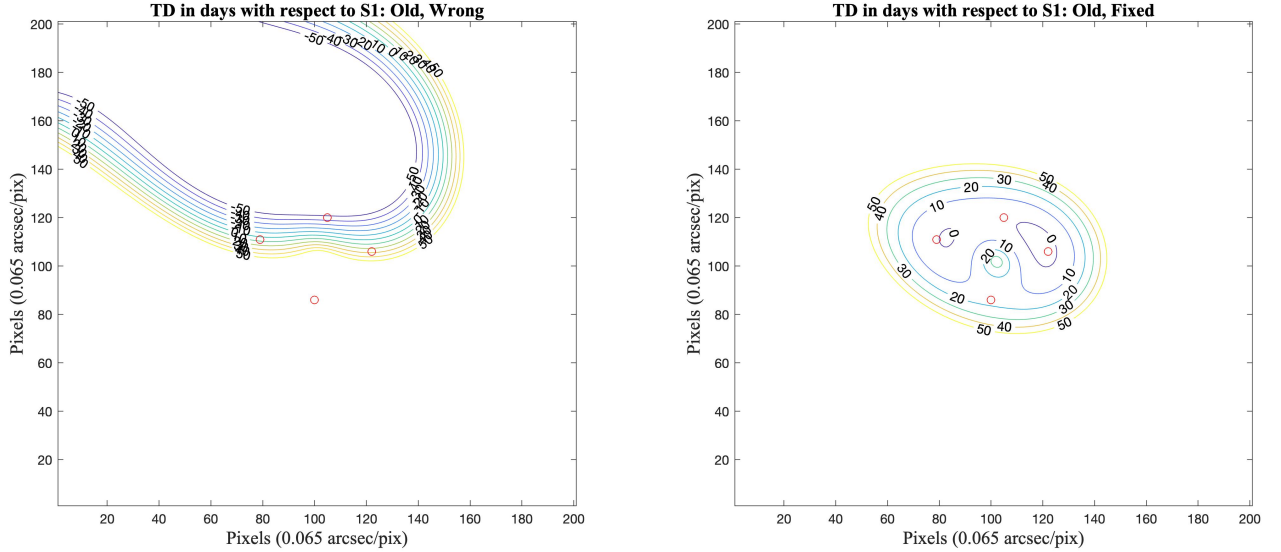


Figure 4. Contours for the TD surface from our old LTM model, in decrements of 10 days. *Left:* Example of the deformed TD surface with the old code in which the potential and deflection fields were not perfectly self-consistent (potential obtained by numerical integration). *Right:* TD surface for the same old model, after correction to the code (the deflection field was taken directly to be the gradient of the (integrated) potential, see text). Red circles mark the positions of the four SN images of the Einstein cross. The TD surface from our new model presented in this work is shown in Fig. 2. and the relevant values are listed in Table 1.

TD [68.3%][95%], 224.4 [221.4 – 272.7] [197.8 – 305.5] days, is the one that would have been given prior to the detection of SX, had we used the current model – and it seems that it matches almost exactly the old LTM TD estimate in Kelly et al. (2016), but with a lower SX/S1 magnification ratio.

Finally, we briefly mention that, by design, the range of different trial models we constructed in the process of re-modeling M1149 (specifically models with $\text{rms} < 1''$),

spanning a range of input configurations (number of freely weighted galaxies and which, ellipticity of the BCGs, number of systems with free redshifts, etc.), typically fall within the range of errors for our best-fit model presented in Table 1. The majority of these models give values for the SX-S1 TD of ~ 170 days to ~ 340 days, most concentrated around 200-260 days, but few – usually the less well constrained models – give larger or smaller TDs.

Table 1. Time Delays and Magnification ratios for SN Refsdal

Parameter	$\Delta t(t)$	$\Delta t(p)$	LTM ^c [68.3% CI] [95% CI]	LTM ^d [68.3% CI] [95% CI]
$\Delta t_{S2:S1}$	4 ± 4^a	7 ± 2^a	5.4 [3.3 – 6.4] [2.8 – 7.2]	2.3 [0.8 – 5.2] [-0.2 – 7.1]
$\Delta t_{S3:S1}$	2 ± 5^a	0.6 ± 3^a	1.6 [0.8 – 2.1] [0.6 – 2.9]	-10.0 [-11.5 – -2.8] [-12.9 – -0.43]
$\Delta t_{S4:S1}$	24 ± 7^a	27 ± 8^a	26.3 [23.4 – 27.4] [22.6 – 28.3]	12.9 [10.8 – 19.5] [7.75 – 22.2]
$\Delta t_{SX:S1}$	345 ± 10^b	345 ± 10^b	224.4 [221.4 – 272.7] [197.8 – 305.5]	267.4 [263.1 – 305.3] [249.8 – 320.3]
$\Delta t_{SY:S1}$	—	—	-6522 [-6623 – -6137] [-6834 – -6025]	-6335 [-6479 – -6083] [-6776 – -5768]
μ_{S2}/μ_{S1}	1.15 ± 0.05^a	1.17 ± 0.02^a	0.86 [0.69 – 1.34] [0.45 – 1.57]	(0.86 [0.69 – 1.34] [0.45 – 1.57])
μ_{S3}/μ_{S1}	1.01 ± 0.04^a	1.00 ± 0.01^a	0.94 [0.88 – 1.00] [0.78 – 1.09]	(0.94 [0.88 – 1.00] [0.78 – 1.09])
μ_{S4}/μ_{S1}	0.34 ± 0.02^a	0.38 ± 0.02^a	0.23 [0.19 – 0.32] [0.14 – 0.36]	(0.23 [0.19 – 0.32] [0.14 – 0.36])
μ_{SX}/μ_{S1}	0.28 ± 0.1^b	0.28 ± 0.1^b	0.21 [0.19 – 0.23] [0.16 – 0.25]	(0.21 [0.19 – 0.23] [0.16 – 0.25])
μ_{SY}/μ_{S1}	—	—	0.15 [0.13 – 0.17] [0.11 – 0.18]	(0.15 [0.13 – 0.17] [0.11 – 0.18])

NOTE—Early measurements of SN Refsdal’s TDs (in days) and magnification ratios, along with estimates from our new LTM model. Note that TDs and magnifications were not used as constraints in the minimization, and similarly, any information regarding SX (and SY) was not used explicitly as well. We expect more accurate measurements of SN Refsdal’s properties will become available in the future.

^a - Taken from Table 3 in [Rodney et al. \(2016b\)](#) based on a set of templates (t), or on polynomials (p) [this notation is adopted from [Grillo et al. \(2018\)](#)].

^b - Taken from [Grillo et al. \(2018\)](#), adopted therein following Fig. 3 in [Kelly et al. \(2016\)](#). In practice, the 1σ uncertainties in [Kelly et al. \(2016\)](#) are closer to 10%.

^c - Source position taken as mean of the delensed positions of the Einstein cross images, S1-S4. These values are those relevant for the properties of the four Einstein cross images.

^d - Source position taken as mean of delensed position of five images: the Einstein cross images, S1-S4 and the position of SX.

The magnification values are independent of the exact source position.

4.2. Comparison with the older model

Differences with respect to our older LTM models that appeared in [Treu et al. \(2016\)](#), [Rodney et al. \(2016b\)](#), and [Kelly et al. \(2016\)](#), can be divided into three main categories: differences in the input and the constraints that were used, minor corrections to the code, and the TD calculation fix.

One difference in input between the older model and the current one, although perhaps not very significant, is that we rerun the photometry of cluster members to create a new member galaxy catalog. Some minor differences exist also for the constraints: in the previous model all multiple image families in the gold list were used except system 14, and a partial list of knots of the spiral galaxy were used, whereas here we use the full gold list (with few silver images in gold systems) and including the full list of knots from [Finney et al. \(2018\)](#), see also [Treu et al. \(2016\)](#)). Systems with no spectroscopic redshift were previously left to be freely optimized in the old model, whereas here these systems (namely systems 6, and 7) were kept fixed on their typical best-fit photometric redshift, $z \simeq 2.6$. Image position uncertainties were adopted to be $0.5''$ for most systems also in the

older model, and for the four SN images for which $0.15''$ was used previously, we now used $0.1''$.

One technical difference between the older model and the current one is that the efficiency of the code was slightly improved, so it could be actually run in the native HST resolution whereas before it was typically run with a few times lower resolution and then interpolated to the native pixel scale (or with higher resolution but less MC steps).

Several other minor corrections to the code have taken place since our 2014 model, but there was no significant change to the modeling scheme. The main improvement in the current model estimates, however, is the fix in the TD calculation part. Thanks to the blind comparison undertaken for SN Refsdal ([Treu et al. 2016](#); [Rodney et al. 2016b](#); [Kelly et al. 2016](#)), we detected a problem in the previously submitted TD surface: the SN images did not seem to form at the extrema of the Fermat surface as expected (see Fig. 8 in [Treu et al. \(2016\)](#), Fig. 4 left here). After investigating the origin of the problem, we reached the following conclusion – and corresponding fix. In the LTM formalism many of the operations are performed in Fourier space for speed up purposes. For example, the deflection fields are calculated in Fourier

space, and since in our scheme the potential cannot be calculated analytically or parametrically from the mass map (or deflection field), it is instead derived by integrating, in Fourier space, the mass density distribution times the log of the distance to each point (see eq. 51 in Narayan & Bartelmann 1996). The potential due to the external shear is then added analytically onto the same grid to obtain the total potential. The total potential was then used together with the deflection fields to estimate the TD surface. The problem was that the gradient of this potential resulted in deflection field components (or if differentiated again, kappa maps) that were verified to be overall very similar to the original deflection fields or kappa map that were integrated to begin with, but in fact were not *exactly* the same (see Fig. 3). Dividing the original deflection fields and kappa map by their parallels obtained via the potential, we get that the mean of the division maps is $\simeq 1$ to within 1% in all cases, but that about 5-10% of the pixels in each division map are outliers, differing by more than 5% or 10%, respectively. This discrepancy caused the TD surface to deform (Fig. 4 left; the effect is similar, essentially, to shifting the source position). To fix this we simply override the "original" deflection field in each step with the deflection field obtained by taking the gradient of the potential. Hence, the potential in each step now constitutes the new starting point, from which all components of the model are then self-consistently deduced. With this the TD surface, *including of our older model submitted to the original comparison test*, forms where expected with the SN images in its extrema.

It should also be mentioned that in retrospect, the error could have been in principle found also without SN Refsdal, just by examining the TD surface on small scales or with sufficiently detailed self-consistency tests. In practice, however, it was the blind comparison and more importantly the fact that our older results for the Einstein cross (i.e., on small scales especially; Rodney et al. 2016b) were outliers, that made us notice this issue, eventually.

4.3. Implications for the Hubble constant

The TD equation is given by (e.g., eq. 63 in Narayan & Bartelmann 1996):

$$t(\vec{\theta}) = \frac{1+z_l}{c} \frac{D_l D_s}{D_{ls}} \left[\frac{1}{2} (\vec{\theta} - \vec{\beta})^2 - \psi(\vec{\theta}) \right] \quad (1)$$

where $\vec{\theta}$ is the image position, $\vec{\beta}$ is the source position as indicated by the lens model, and ψ the gravitational potential given by the lens model. D_l , D_s , and D_{ls} are the angular diameter distances to the lens, to the source, and between the lens and the source, respectively. The

above equation describes the delayed arrival time of each image compared to an undeflected light ray from the same source had there not been any intervening lens, and we denoted the arrival time difference between the different multiple images simply as the TD. The combination of angular diameter distances, $\frac{D_l D_s}{D_{ls}}$ – sometimes called the TD distance, especially if including the $(1+z_l)$ factor as well – is inversely proportional to the Hubble constant. Hence, using eq. 1, by comparing observed TDs with the TDs expected from a lens model that was constructed using the positions of the multiple images (note the model is independent of the Hubble constant; the latter only enters when estimating the TD), an estimate of the true underlying Hubble constant can be derived. The TD distance depends much more mildly also on the cosmological parameters (Grillo et al. 2020), and a full statistical treatment is needed for proper constraints on the Hubble constant, to include the explicit statistical uncertainties from both the model and TD measurement. Nevertheless, one can obtain a rough estimate by simply rescaling the model's TD using the measured TD:

$$H_{0,true} = \text{TD}_{model} / \text{TD}_{true} \cdot H_{0,model} \quad (2)$$

where we used in our modeling $H_{0,model} = 70$ km/s/Mpc. The final, "true" measured TD for Refsdal is yet unknown at the time of writing. If, for example, we use the $\text{TD}_{true} = 345 \pm 10$ between S1 and SX adopted by Grillo et al. (2018), the Hubble constant implied by our model would be as low as ~ 46 km/s/Mpc, with a 95% CI of $\simeq [40 - 62]$ km/s/Mpc, in the case where the cross' source position is adopted; or ~ 54 km/s/Mpc with a 95% CI of $\simeq [51 - 65]$ km/s/Mpc, in the case where the mean cross+SX source position is adopted. However if the final measured TD would be around 220-270 days (this can be the case if the magnification of SX were sufficiently low), then the Hubble constant would be around 70 km/s/Mpc (for the two source positions, respectively), as is measured from other probes and other TD systems as well. For previous measurements of the Hubble constant with SN Refsdal we refer the reader to Vega-Ferrero et al. (2018) and Grillo et al. (2018), where discussions of possible systematics and the accuracy of the TDs was investigated, for example, by Williams & Liesenborgs (2019), Birrer & Treu (2019) and Grillo et al. (2020).

5. CONCLUSIONS

The main purpose of this paper was to present a long-due revision of our LTM model for M1149, following an inconsistency (a numerical artifact) that was discovered in the TD calculation part of the code. The artifact was

found after noticing that the TD surface of the LTM model we submitted to the SN Refsdal blind challenge in 2015 was deformed, not producing the multiple images at its extrema. We have found that the origin of the problem was a slight inconsistency between the deflection field or kappa maps, and the integrated potential, which led to, effectively, a slightly shifted source position and deformed TD surface. Note that the inconsistency involves only the TD estimates through the calculation of the potential, and as it does not affect the multiple image reproduction or the accuracy of the LTM model more generally, it remained unnoticed (and mostly irrelevant) prior to SN Refsdal. We revise our code to use the potential as starting point in each step so that all lensing quantities are self-consistently derived from it directly. We rerun our model for M1149, presented here, and update the TDs and magnifications for SN Refsdal accordingly. These, in turn, could be compared to updated measurements of SN Refsdal.

If a large discrepancy remains between our current TDs and those measured for SN Refsdal (for example, while they very broadly agree, the LTM predictions for SX-S1 TD in particular, seem to be systematically lower than those from most parametric techniques), it will enable us to test which specific assumptions in our model lead to a distinct TD, and may cast important clues regarding which properties of the underlying matter distribution are crucial for correct TD mapping. In parallel to this paper we also publish a *parametric* model for M1149, to enable a more direct comparison (Zitrin, A., submitted and posted online).

Our work highlights the extended usefulness of blind prediction tests in astronomy.

ACKNOWLEDGEMENTS

This work was made possible by useful discussions with Pat Kelly, Tommaso Treu, and Steve Rodney. I am very grateful for these discussions and for their comments on the manuscript. I am also very grateful for Tommaso Treu’s notice of the deformed TD surface, which led us to examine the origin of the inconsistency, and to fix it. AZ is also grateful for useful discussions and multiple image voting that took place as a community effort in the HFF framework, and to the respective teams that submitted models – led by PIs Bradac, Natarajan & Kneib (CATS), Merten & Zitrin, Sharon, Williams, Keeton, Bernstein and Diego, and the GLAFIC group. The work uses some scripts from the astronomy MATLAB package (Ofek 2014). This work is based on observations obtained with the NASA/ESA Hubble Space Telescope, retrieved from the Mikulski Archive for Space Telescopes (MAST) at the Space Tele-

scope Science Institute (STScI). STScI is operated by the Association of Universities for Research in Astronomy, Inc. under NASA contract NAS 5-26555.

Table 2. Multiple Image Systems

ID	R.A	DEC.	z_{spec}	z_{phot}	Category
1.1	177.39700	22.39600	1.488		Gold
1.2	177.39942	22.39743	1.488		Gold
1.3	177.40342	22.40243	1.488		Gold
1.5	177.39986	22.39713	—		Silver
2.1	177.40242	22.38975	1.891		Gold
2.2	177.40604	22.39247	1.891		Gold
2.3	177.40658	22.39288	1.891		Gold
3.1	177.39075	22.39984	3.129		Gold
3.2	177.39271	22.40308	3.129		Gold
3.3	177.40129	22.40718	3.129		Gold
4.1	177.39300	22.39682	2.949		Gold
4.2	177.39438	22.40073	2.949		Gold
4.3	177.40417	22.40612	2.949		Gold
5.1	177.39975	22.39306	2.80		Gold
5.2	177.40108	22.39382	—	2.6 ± 0.1	Gold
5.3	177.40792	22.40355	—	2.8 ± 0.1	Silver
6.1	177.39971	22.39254	—		Gold
6.2	177.40183	22.39385	—	$2.6^{+0.1}_{-2.3}$	Gold
6.3	177.40804	22.40250	—		Silver
7.1	177.39896	22.39133	—	2.6 ± 0.1	Gold
7.2	177.40342	22.39426	—	$2.7^{+0.1}_{-0.2}$	Gold
7.3	177.40758	22.40124	—	$2.3^{+0.1}_{-0.2}$	Gold
13.1	177.40371	22.39778	1.23		Gold
13.2	177.40283	22.39665	1.25		Gold
13.3	177.40004	22.39385	1.23		Gold
14.1	177.39167	22.40348	3.703		Gold
14.2	177.39083	22.40264	3.703		Gold
110.1	177.40014	22.39016	3.214		Gold
110.2	177.40402	22.39289	3.214		Gold

NOTE—Multiple images used as constraints in the modeling. These systems comprise the Gold sample, as defined in (Treu et al. 2016) following a ranking of the images based on votes from various lensing teams. While some differences exist, generally speaking, these systems were used in constructing the models for the comparison work of SN Refsdal (Treu et al. 2016; Kelly et al. 2016; Rodney et al. 2016a), but some also used the silver sample, not shown in full here. Many of the images in the Table (namely those of systems 1 through 7, and 13) were originally found in our earlier work by previous versions of the LTM model for this cluster (Zitrin & Broadhurst 2009; Zheng et al. 2012; Zitrin et al. 2015, see also (Smith et al. 2009)). Indices, coordinates, and redshifts are taken from Finney et al. (2018), following Treu et al. (2016).

Table 3. Multiply Imaged Knots

ID	R.A	DEC.
1.1.1	177.39702	22.39600
1.1.2	177.39942	22.39743
1.1.3	177.40341	22.40244
1.1.5*	177.39986	22.39713
1.2.1	177.39661	22.39630
1.2.2	177.39899	22.39786
1.2.3	177.40303	22.40268
1.2.4	177.39777	22.39878
1.2.6	177.39867	22.39824
1.3.1	177.39687	22.39621
1.3.2	177.39917	22.39760
1.3.3	177.40328	22.40259
1.4.1	177.39702	22.39621
1.4.2	177.39923	22.39748
1.4.3	177.40339	22.40255
1.5.1	177.39726	22.39620
1.5.2	177.39933	22.39730
1.5.3	177.40356	22.40252
1.6.1	177.39737	22.39616
1.6.2	177.39945	22.39723
1.6.3	177.40360	22.40248
1.7.1	177.39757	22.39611
1.7.2	177.39974	22.39693
1.7.3	177.40370	22.40240
1.8.1	177.39795	22.39601
1.8.2	177.39981	22.39675
1.8.3	177.40380	22.40231
1.9.1	177.39803	22.39593
1.9.2	177.39973	22.39698
1.9.3	177.40377	22.40225
1.10.1	177.39809	22.39585
1.10.2	177.39997	22.39670
1.10.3	177.40380	22.40218
1.11.2	177.40010	22.39666
1.11.3	177.40377	22.40204
1.12.1	177.39716	22.39521
1.12.2	177.40032	22.39692
1.12.3	177.40360	22.40187
1.13.1	177.39697	22.39663

Table 3 *continued***Table 3** (*continued*)

ID	R.A	DEC.
1.13.2	177.39882	22.39771
1.13.3	177.40329	22.40282
1.13.4	177.39791	22.39843
1.14.1	177.39712	22.39672
1.14.2	177.39878	22.39763
1.14.3	177.40338	22.40287
1.14.4	177.39810	22.39825
1.15.1	177.39717	22.39650
1.15.2	177.39894	22.39751
1.15.3	177.40344	22.40275
1.16.1	177.39745	22.39640
1.16.2	177.39915	22.39722
1.16.3	177.40360	22.40265
1.17.1	177.39815	22.39634
1.17.2	177.39927	22.39683
1.17.3	177.40384	22.40256
1.18.1	177.39850	22.39610
1.18.2	177.39947	22.39659
1.18.3	177.40394	22.40240
1.19.1	177.39689	22.39576
1.19.2	177.39954	22.39748
1.19.3	177.40337	22.40229
1.19.5	177.39997	22.39710
1.20.1	177.39708	22.39572
1.20.2	177.39963	22.39736
1.20.3	177.40353	22.40223
1.20.5	177.40000	22.39698
1.21.1	177.39694	22.39540
1.21.3	177.40341	22.40200
1.21.5	177.40018	22.39704
1.22.1	177.39677	22.39548
1.22.2	177.39968	22.39749
1.22.3	177.40328	22.40209
1.22.5	177.40008	22.39713
1.23.1	177.39672	22.39538
1.23.2	177.39977	22.39749
1.23.3	177.40324	22.40201
1.23.5	177.40013	22.39720
1.24.1	177.39650	22.39558
1.24.2	177.39953	22.39775
1.24.3	177.40301	22.40220

Table 3 *continued*

Table 3 (*continued*)

ID	R.A	DEC.
1.25.1	177.39657	22.39593
1.25.3	177.40304	22.40245
1.26.1	177.39633	22.39601
1.26.3	177.40283	22.40260
1.27.1	177.39831	22.39628
1.27.2	177.39933	22.39672
1.28.1	177.39860	22.39616
1.28.2	177.39942	22.39655
1.29.1	177.39858	22.39586
1.29.2	177.39976	22.39649
1.30.1	177.39817	22.39546
1.30.2	177.39801	22.39523
1.30.3	177.39730	22.39536
1.30.4	177.39788	22.39572
SN1	177.39823	22.39563
SN2	177.39772	22.39578

SN3	177.39737	22.39553
SN4	177.39781	22.39518
SX* ^a	177.40024	22.39681
SY* ^a	177.40380	22.40214

NOTE—In addition to the multiple image systems above, we also use individual, multiply imaged knots in the lensed spiral hosting Refsdal ($z = 1.49$) as constraints. Also here the IDs and coordinates follow Finney et al. (2018), based on Treu et al. (2016).

* Images with an asterisk are shown for completeness and were not used in the minimization.

^a Note that for SX and SY there seems to be some discrepancy between the listed coordinates (taken from Finney et al. (2018)) and those we measure in the data ourselves.

REFERENCES

- Baklanov, P., Lyskova, N., Blinnikov, S., & Nomoto, K. 2020, arXiv e-prints, arXiv:2007.04106
- Bertin, E., & Arnouts, S. 1996, *A&AS*, 117, 393
- Birrer, S., & Treu, T. 2019, *MNRAS*, 489, 2097
- Blandford, R., Dunkley, J., Frenk, C., Lahav, O., & Shapley, A. 2020, *Nature Astronomy*, 4, 122
- Broadhurst, T., Benítez, N., Coe, D., et al. 2005, *ApJ*, 621, 53
- Carrasco, M., Zitrin, A., & Seidel, G. 2020, *MNRAS*, 491, 3778
- Carvajal, R., Bauer, F. E., Bouwens, R. J., et al. 2020, *A&A*, 633, A160
- Chen, M. C., Broadhurst, T., Lim, J., et al. 2018, *ApJ*, 863, 135
- Chen, W., Kelly, P. L., Diego, J. M., et al. 2019, *ApJ*, 881, 8
- Della Costa, John, I., Sarajedini, V. L., & Strolger, L.-G. 2020, arXiv e-prints, arXiv:2003.11035
- Diego, J. M., Broadhurst, T., Chen, C., et al. 2016, *MNRAS*, 456, 356
- Diego, J. M., Kaiser, N., Broadhurst, T., et al. 2018, *ApJ*, 857, 25
- Ebeling, H., Barrett, E., Donovan, D., et al. 2007, *ApJL*, 661, L33
- Emami, N., Siana, B., Alavi, A., et al. 2020, *ApJ*, 895, 116
- Finney, E. Q., Bradač, M., Huang, K.-H., et al. 2018, *ApJ*, 859, 58
- Freedman, W. L., Madore, B. F., Hatt, D., et al. 2019, *ApJ*, 882, 34
- González-López, J., Bauer, F. E., Romero-Cañizales, C., et al. 2017, *A&A*, 597, A41
- Goobar, A., Amanullah, R., Kulkarni, S. R., et al. 2017, *Science*, 356, 291
- Grillo, C., Rosati, P., Suyu, S. H., et al. 2020, arXiv e-prints, arXiv:2001.02232
- . 2018, *ApJ*, 860, 94
- Hashimoto, T., Laporte, N., Mawatari, K., et al. 2018, *Nature*, 557, 392
- Ishigaki, M., Kawamata, R., Ouchi, M., et al. 2018, *ApJ*, 854, 73
- Janssens, S. R., Abraham, R., Brodie, J., Forbes, D. A., & Romanowsky, A. J. 2019, *ApJ*, 887, 92
- Johnson, T. L., Sharon, K., Bayliss, M. B., et al. 2014, *ApJ*, 797, 48
- Kaurov, A. A., Dai, L., Venumadhav, T., Miralda-Escudé, J., & Frye, B. 2019, *ApJ*, 880, 58
- Kawamata, R., Oguri, M., Ishigaki, M., Shimasaku, K., & Ouchi, M. 2016, *ApJ*, 819, 114
- Kelly, P. L., Rodney, S. A., Treu, T., et al. 2015, *Science*, 347, 1123
- . 2016, *ApJL*, 819, L8
- Kelly, P. L., Diego, J. M., Rodney, S., et al. 2018, *Nature Astronomy*, 2, 334

- Lotz, J. M., Koekemoer, A., Coe, D., et al. 2017, *ApJ*, 837, 97
- Muñoz Arancibia, A. M., González-López, J., Ibar, E., et al. 2018, *A&A*, 620, A125
- Narayan, R., & Bartelmann, M. 1996, *ArXiv Astrophysics e-prints*, astro-ph/9606001, arXiv:astro-ph/9606001
- Ofek, E. O. 2014, *MATLAB package for astronomy and astrophysics*, ASCL Code Record, ascl:1407.005
- Oke, J. B., & Gunn, J. E. 1983, *ApJ*, 266, 713
- Planck Collaboration, Aghanim, N., Akrami, Y., et al. 2018, *arXiv e-prints*, arXiv:1807.06209
- Postman, M., Coe, D., Benítez, N., et al. 2012, *ApJS*, 199, 25
- Quimby, R. M., Werner, M. C., Oguri, M., et al. 2013, *ApJL*, 768, L20
- Quimby, R. M., Oguri, M., More, A., et al. 2014, *Science*, 344, 396
- Rau, S., Vegetti, S., & White, S. D. M. 2014, *MNRAS*, 443, 957
- Refsdal, S. 1964, *MNRAS*, 128, 307
- Richard, J., Jauzac, M., Limousin, M., et al. 2014, *MNRAS*, 444, 268
- Riess, A. G., Casertano, S., Yuan, W., Macri, L. M., & Scolnic, D. 2019, *ApJ*, 876, 85
- Rodney, S. A., Strolger, L. G., Kelly, P. L., et al. 2016a, *ApJ*, 820, 50
- Rodney, S. A., Strolger, L.-G., Kelly, P. L., et al. 2016b, *ApJ*, 820, 50
- Rodney, S. A., Balestra, I., Bradac, M., et al. 2018, *Nature Astronomy*, 2, 324
- Smith, G. P., Ebeling, H., Limousin, M., et al. 2009, *ApJL*, 707, L163
- Steinhardt, C. L., Jauzac, M., Acebron, A., et al. 2020, *ApJS*, 247, 64
- Suyu, S. H., Auger, M. W., Hilbert, S., et al. 2013, *ApJ*, 766, 70
- Treu, T., Schmidt, K. B., Brammer, G. B., et al. 2015, *ApJ*, 812, 114
- Treu, T., Brammer, G., Diego, J. M., et al. 2016, *ApJ*, 817, 60
- Vega-Ferrero, J., Diego, J. M., Miranda, V., & Bernstein, G. M. 2018, *ApJL*, 853, L31
- Vuissoz, C., Courbin, F., Sluse, D., et al. 2008, *A&A*, 488, 481
- Wang, X., Jones, T. A., Treu, T., et al. 2017, *ApJ*, 837, 89
- Williams, L. L. R., & Liesenborgs, J. 2019, *MNRAS*, 482, 5666
- Wong, K. C., Suyu, S. H., Chen, G. C. F., et al. 2019, *arXiv e-prints*, arXiv:1907.04869
- Zalesky, L., & Ebeling, H. 2020, *MNRAS*, arXiv:2007.12182
- Zheng, W., Postman, M., Zitrin, A., et al. 2012, *Nature*, 489, 406
- Zheng, W., Zitrin, A., Infante, L., et al. 2017, *ApJ*, 836, 210
- Zitrin, A., & Broadhurst, T. 2009, *ApJL*, 703, L132
- Zitrin, A., Broadhurst, T., Umetsu, K., et al. 2009, *MNRAS*, 396, 1985
- Zitrin, A., Fabris, A., Merten, J., et al. 2015, *ApJ*, 801, 44